Development of a Miniature Embedded Imaging System for Internal Flow Measurements

G. Eagan[1,*], C. Lewis[2], R. Alles[1], B. Rice[3], M. Hamilton[2], B. Thurow[1]

1: Dept. of Aerospace Engineering, Auburn University, United States
2: Dept. of Electrical and Computer Engineering, Auburn University, United States
3: AFRL AEDC, United States
*Corresponding author: gde0003@auburn.edu

Keywords: Internal Flow Measurement, PSP, Oil Flow Visualization

ABSTRACT

Through this work, the foundation has been laid for the development of a system for small-scale, integrated, image-based flow diagnostics for ground and flight tests. This system addresses many of the challenges associated with alternative methods of performing these measurements. For this work a 120 fps imager was embedded in the ceiling of a Mach 2.0 wind tunnel to perform oblique shock impingement measurements. Illumination was provided via a ring-light system of micro-LEDs embedded around the camera lens aperture. The entire system was controlled using a Raspberry Pi 4 Model B to capture and process image data. The integrated system possesses a total aperture diameter of 20 mm. Pressure sensitive paint and UV oil flow visualization experiments capturing an oblique shock/boundary layer interaction were performed using this system.

1. Introduction

High-speed, internal flow field measurements present a number of logistical challenges. Optical access is usually limited or non-existent. Testing environments are harsh, typically involving conditions at the extremes of pressure, temperature and vibration. Ground test facilities often necessitate long working distances, introducing a whole host of optical considerations and trade offs. Model motion due to aerodynamic loads during runs, particularly unsteady loads, complicates data analysis. Run times in many academic facilities are extremely short, being measured in milliseconds or seconds rather than minutes. Some attempts have been made to circumvent these issues. Researchers have split models along a line of symmetry to improve optical access, instead inducing flow deformation not present in the original model. (Tsukahira et al., 1971) Others have manufactured entirely transparent models, improving optical access and instead introducing added optical refraction that must be accounted. (Emami et al., 1995; Wagner, 2009) These approaches alleviate some of the challenges listed previously, but not all, and often induce other issues in the process.

An alternate solution is introduced here. A great deal of progress has been made in the field of micro-imaging. Cell phone cameras are smaller than ever, with high resolutions and high frame rates. A novel diagnostic system has been developed as part of the present work which leverages the advances in this field. A miniature, board-mounted camera system has been developed which is designed to be embedded directly into test articles and/or wind tunnel walls, alleviating a great deal of the present limitations associated with performing internal flow measurements.

The resulting camera system has been embedded into the ceiling of a small wind tunnel test section to simulate the sort of internal flowfield measurements and length scales associated with many production-level ground test facilities. A wedge test article was placed upstream of the camera to generate an impinging oblique shock system. Measurements of this internal flow field were obtained by performing pressure sensitive paint (PSP) and ultraviolet oil flow visualization (UV OFV) experiments.

2. Experimental Setup

Presented below is an implementation of a packaged embedded camera system designed to perform optically-based experiments. Objectives of the system were to minimize size, to simplify integration, and to possess a high frame rate and high resolution. The primary challenges associated with the development of this system were development of a compact, all-in-one package with adequate temporal and spatial resolution for measurement fidelity and also producing a cost-efficient, modular solution for offloading and processing image data.

2.1. Imaging System

At the heart of the imaging system is the image sensor. A number of different considerations must be made when selecting an image sensor for a particular application. For the purposes of making time-dependent, empirical measurements, a high resolution, high frame rate, global shutter image sensor is desirable. For this particular application it was also desirable to maximize these parameters while achieving a minimum optical format to maintain the small size of the camera system. The primary tradeoff in current image sensor offerings is between resolution and optical format. This relationship is depicted below in Figure 1 for image sensor offerings from Omnivision and Sony.(Omnivision, 2020; Sony, 2020) As can be seen from this figure, the typical rolling shutter image sensor possesses a smaller optical format than the equivalent resolution global shutter image sensor.

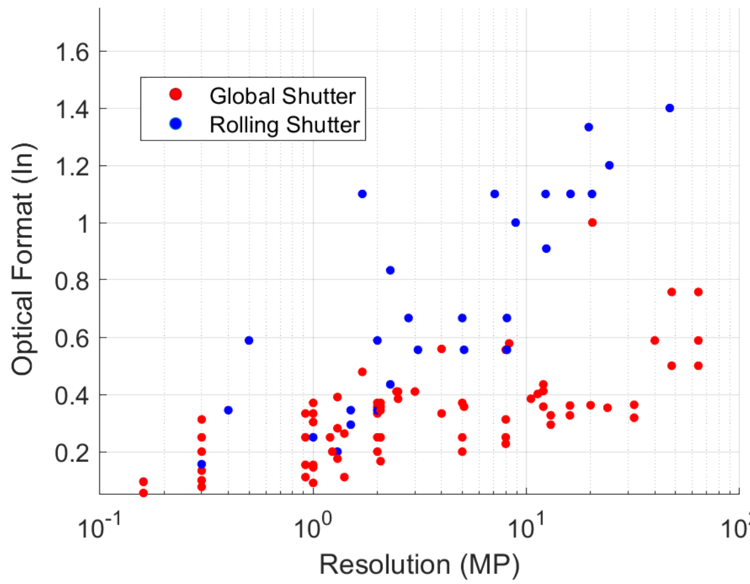

Figure 1. Plot of resolution versus optical format for various global shutter and rolling shutter image sensors

Based on these findings, the Omnivision OV9281 image sensor was selected for use in these experiments to maximize resolution and frame rate without incurring a substantial increase in optical format. This image sensor was mounted onto a module board produced by Arducam which permitted the use of standard M12 lenses.(Arducam, 2020) An example of this camera module is shown below in Figure 2. Image data is output from the camera module across two MIPI-compliant data lanes via a 22-pin flat ribbon cable that is compatible with most Raspberry Pis. This module is capable of accepting an external trigger and providing a flash pulse to and from the sensor. Table 1 shows the key specifications for this image sensor.

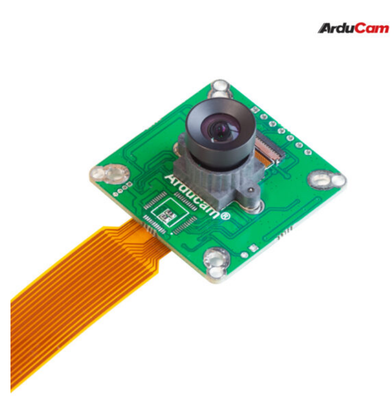

Figure 2. MIPI camera module produced by Arducam

Table 1. Arducam OV9281 image sensor module specifications

Resolution	1280 x 800
Frame Rate	120 fps
Output Interface	2-lane MIPI
Pixel Size	$3\ \mu m$ x $3\ \mu m$
Optical Size	6.35 mm
Output Format	RAW8/10
Module Dimensions	40mm x 40mm
Lens Type	M12

The housing for this camera module was designed with the primary objective of simplifying camera integration into into wind tunnel walls or test articles. A depiction of the completed camera housing is shown in Figure 3. In this figure, the aluminum camera housing, integrated LED array, optical filter, camera lens, window and wiring can be seen. All the aforementioned components are consumer, off-the-shelf (COTS) with the exception of the aluminum housing and the printed circuit board (PCB) where the LEDs are mounted. The lens is an Arducam M12-mount lens with a 45° field of view and manually adjustable working depth. Integrated illumination is provided by a ring light array of 40 410 nm 0603-format UV LEDs. The total optical power of the array is 400 mW. A 12.5 mm diameter, 600 nm longpass filter placed in front of the camera lens aperture blocks this light from reaching the image sensor. The window is MgF_2-coated BK7 with a thickness of 3 mm and a diameter of 20 mm. The window is adhered to the camera housing using Norland Optical Adhesive NOA 61 which is a UV-cured, optically-clear adhesive with exceptional bonding between glass and metal. The entire package is approximately 25 mm cubic in size. Installation of the housing is achieved by machining of a single thru-hole and a pattern of 4 tapped holes into a wind tunnel or test article wall.

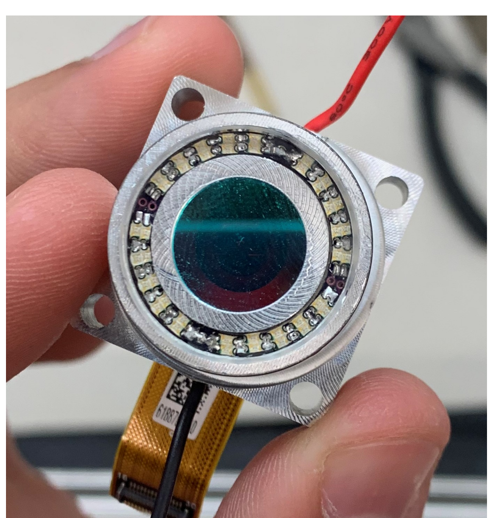

Figure 3. Front view of fully assembled camera housing

Control of the camera module and data processing and storage are performed via a Raspberry Pi 4 Model B. This system also simultaneously controls the integrated lighting system within the camera housing. Figure 4 displays a block diagram depicting this control system. A python script was used to control the camera module and lighting system. This script interfaced with the module and data via driver software provided by Arducam. Power for the lighting system was provided externally via an Agilent E3642A DC power supply and relay system. Once a trigger signal was received by the relay, power was supplied to the LED array at the desired power level. The illumination intensity was controlled by varying input voltage to the LED array while operating the external power supply in a constant current mode. The ring light power system was programmed to turn off automatically at the end of data collection to avoid over exposing the PSP or risking thermal failure in the LED array.

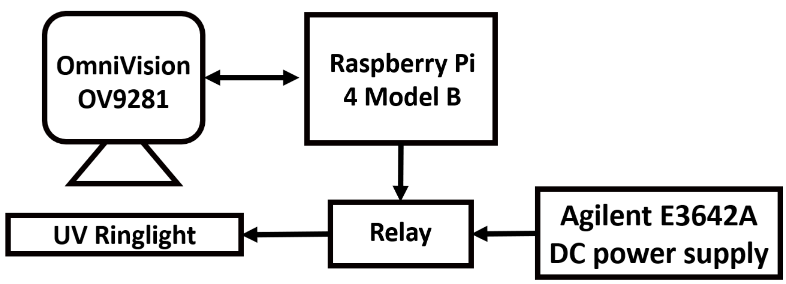

Figure 4. Block diagram of the imaging system

2.2. Facility Description

Preliminary experiments used to assess the performance of the camera system and experimental methods were conducted in the Auburn University Mach 2.0 Wind Tunnel.(Davis, 2013) A schematic of the facility is shown in Figure 5. In this figure the flow planarization inlet and settling chamber flange are shown at far left. Downstream are the transparent nozzle and test section followed by the diffuser section and finally the exhaust outlet on the far right. This facility has a 101.6 mm x 88.9 mm x 355.6 mm test section with acrylic sidewalls for optical access. This optical access was not necessary for these experiments and is a luxury which is typically not available in the design use-case of a production level wind tunnel environment. The test section floor and ceiling are made of removable aluminum plates. This permitted complete control over camera and shock generator placement for the present experiments. Stagnation pressure in this tunnnel may be varied, however the maximum stagnation pressure of 652.9 kPa was used for these experiments. The maximum run time is approximately 10 seconds at this condition.

During the system development phase of this work, the ceiling of the wind tunnel test section was modified to include a rectangular slot. This slot was designed to accept an aluminum insert with a gasket arrangement to seal the joint between the two components. This insert system permitted the rapid alteration of camera mounting and aperture holes as housing dimensions changed throughout the iterative design process.

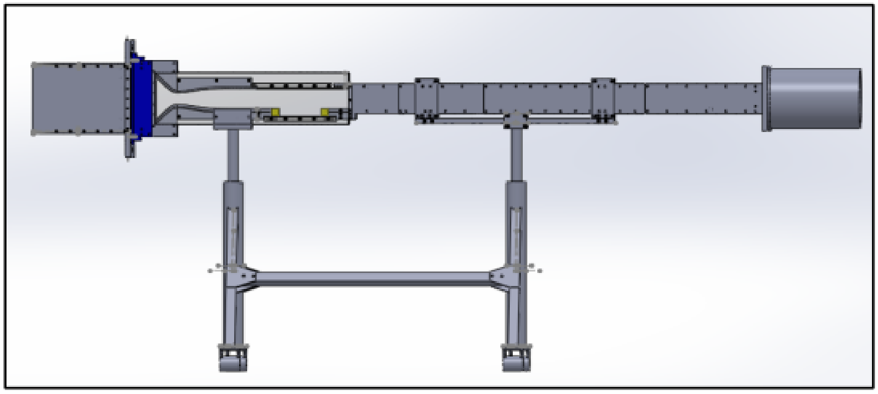

Figure 5. The Auburn University Mach 2 Wind Tunnel

The test article for these experiments consisted of a 20 degree, 19 mm width aluminum wedge. This wedge was suspended from the tunnel ceiling to generate an oblique shock impinging on the tunnel floor within the field of view of the camera. The support for this wedge was a separate piece allowing for gross height adjustment of the wedge in order to be able to alter the impingement location along the floor. A schematic of the experimental arrangement is shown below in Figure 6 and a table of relevant inviscid shock and tunnel flow characteristics is shown in Table 2.

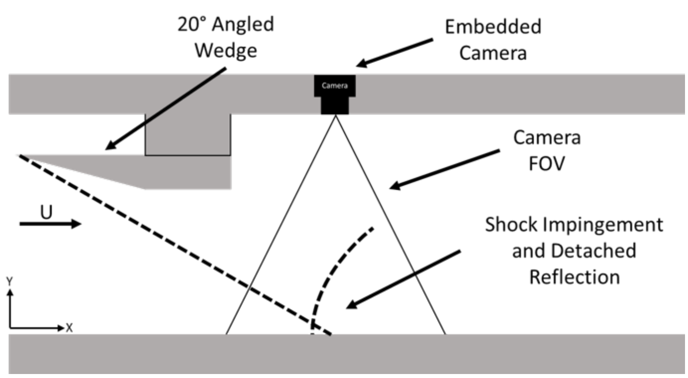

Figure 6. Schematic showing centerline of wind tunnel test section with camera and test article

Table 2. Tunnel and impinging shock characteristics

M	2.0
Re_L	78,555/m
P_2/P_1	2.84
P/P_0	0.127
θ	20.0 deg
β	53.4 deg
AR	1.14

2.3. Experimental Diagnostics

2.3.1. UV-OFV

UV OFV experiments were performed using polydimethylsiloxane (PDMS) silicone oil and Smooth-On Silc Pig Electric fluorescent silicone pigment at a ratio of 16:1 by volume. The viscosity of PDMS remains relatively constant across a wide range of temperatures with a viscosity thermal coefficient of 0.655. Additionally, a wide range of viscosities are available with the same chemical formulation enabling the same basic mixture to be used across a wide range of applications. For these experiments, PDMS with a viscosity of 100 cSt was used. The orange pigment of silicone colorant was selected to maximize contrast in experimentation. Prior to experiments, the tunnel floor insert was prepared by applying matte black paint via aerosol spray. This coating was allowed to dry, at which point the oil and pigment mixture was liberally applied to the surface and installed for testing. During testing the bulk of the oil was washed downstream allowing the shear field to be visualized.

2.3.2. PSP

PSP experiments were performed using a single-component PSP produced by Innovative Scientific Solutions, Inc. (ISSI).(Innovative Scientific Solutions, 2020) This particular PSP is considered slow acting with a response time of 750 ms. A tunnel floor insert was prepared by cleaning with acetone prior to application of the PSP. The PSP was applied to the entire exposed section of tunnel floor via aerosol spray. Five layers of paint were applied in keeping with manufacturer recommendations. The prepared tunnel floor is shown below in Figure 7.

Figure 7. Tunnel floor insert prepared with PSP

Illumination for both the PSP and UV OFV experiments was supplied using the previously described UV ring light integrated into the camera housing.

2.4. Data Analysis

2.4.1. UV-OFV

The data obtained from the UV oil flow visualization experiments was transformed from raw video to individual frames and contrast stretched to aid in flow feature identification. PIV cross-correlation was performed in DaVis 8.4 to extract streamline data for a series of consecutive frames. Conclusions about the features of the flowfield were drawn based on close inspection of the raw images and the streamline results.

2.4.2. PSP

To correct for any fixed pattern noise, ambient lighting conditions, and experimental illumination variances in the raw PSP data, the image flattening procedure described by Equation 1 was applied to the dataset.

$$I_{corrected}(m,n) = \frac{I_{Experimental}(m,n) - I_{Ambient}(m,n)}{I_{WindOff}(m,n) - I_{Ambient}(m,n)} \tag{1}$$

$I_{Experimental}$ is an experimental (light-on-flow-on) image. $I_{Ambient}$ is a median of a series of ambient lighting or light-off-flow-off images to account for any ambient illumination. Finally, $I_{WindOff}$ is a median image with on-board illumination (light-on-flow-off) in use to account for any variations in illumination via this system.

It is necessary to perform pressure calibration following image intensity correction. It is common practice to use either a linear or a second order calibration for PSP data.(Jahanmiri, 2011) A linear calibration method was used for these experiments. The equation for linear PSP calibration is given below in Equation 2.

$$P(m,n) = \frac{P_2 - P_1}{I_2 - I_1} I(m,n) + \frac{P_1 - \frac{I_1}{I_2} P_2}{1 - \frac{I_1}{I_2}} \tag{2}$$

I_1 and I_2 are the image sensor intensities at pressures P_1 and P_2 respectively, and $P(m,n)$ is the resulting calibrated pressure. An in-situ calibration method was used to calibrate the data. For this method, isentropic flow relations were used to estimate the pressure upstream of the oblique shock interaction using the flow Mach number and stagnation pressure. The corresponding pressure is approximately 83 kPa. This pressure, taken as P_2, was correlated to the corrected image intensity in the region upstream of the SBLI. A windowed average image intensity was used to limit pressure measurement uncertainty. Data was obtained prior to tunnel start-up for the image flattening processing step described previously. This measurement prior to tunnel start-up was assumed to be at atmospheric pressure, 101.3 kPa. This was taken as pressure data point P_1 with a normalized intensity of 1.0. A Gaussian blurring was applied to the final calibrated image to reduce image noise and aid in bulk flow feature identification.

3. Results & Discussion

3.1. UV-OFV

Oil flow visualization results from the experiments performed in the Auburn Mach 2.0 Wind Tunnel Facility are shown below in Figure 8. The flow is left to right.

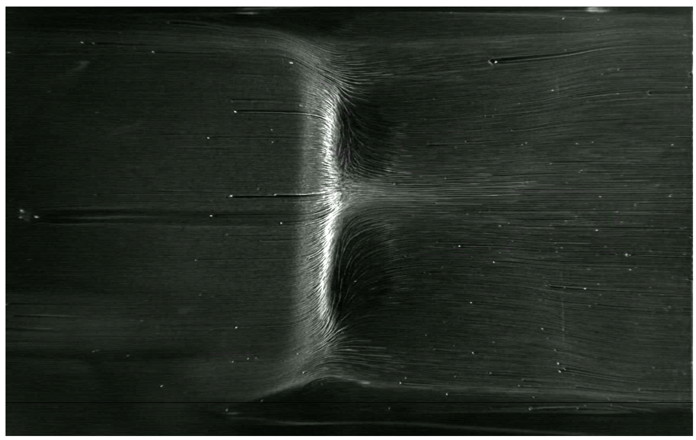

Figure 8. Oil flow visualization of an oblique shock impingement at Mach 2.0

The centerline separation onset appears to be weakly three-dimensional while regions away from the centerline exhibit a great deal of transverse flow. The shock impingement near the centerline and resulting flow momentum loss is made up for by the strong turning of fluid towards this centerline separated region. Thus, the concentration of oil in this region increases and streaklines at other transverse locations are oriented almost perpendicular to the original flow direction. A precise shock reattachment point is difficult to pinpoint from this data. While the region where flow regains downstream momentum is clear, the upstream separated region is probably best described as a region of quasi-separated flow. Downstream of the primary shock impingement streamwise momentum is lost, however no true flow reversal characteristic of flow separation occurs in the bulk of the flow field. It is likely that the flow towards the centerline does recirculate to some degree however this is largely a matter of conjecture due to the large amount of pooled oil in this area. The corner flow separation can be seen here plainly as a protrusion into the main body of the flow at both the top and bottom of the image. The vertex of the corner flow separation on either side of the duct coincides with the primary shock impingement. After this point, the corner flow turns away from the centerline. This induces a pair of symmetric regions of expanding flow propagating towards the tunnel centerline. Downstream, the turning interaction of these two expansion fans is counteracted by the formation of a pair of oblique shocks turning the flow back inline with the original flow direction, in essence forming a shock diamond-like flowfield. A region of attached flow is apparent between the primary separation region and the corner flow separation region. This attached flow region is heavily influenced by both the centerline and corner flow regions. The trends noted for the centerline separation are corroborated by the streamline data shown in Figure 9. The contours are colored by transverse velocity. Based on these results, no centerline recirculation is indicated. The trends noted in the corner flow region and downstream of the oblique shock impingement are not captured. This is likely due to poor oil circulation in these regions resulting in little movement that might be detected from PIV cross-correlation.

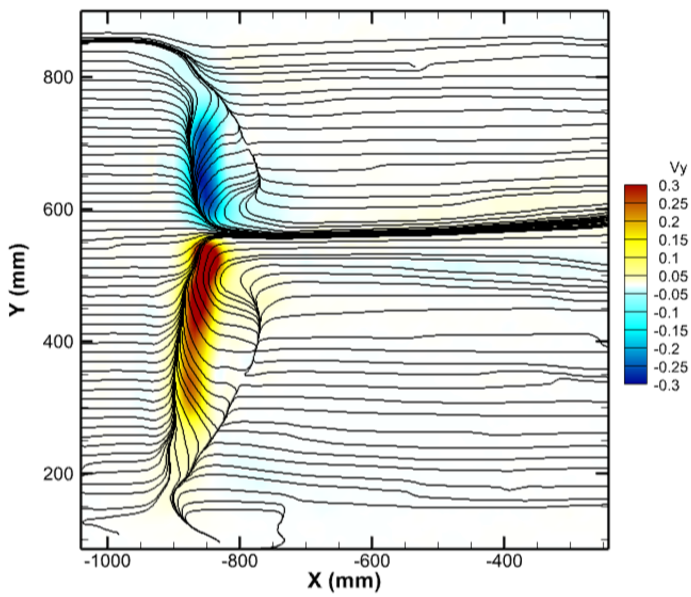

Figure 9. Streamlines extracted from the oil flow visualization results

The general shock-expansion flowfield described above is overlaid on the shear field in Figure 10. This proposed shock interaction was produced in consideration of the results of previous research in similar flowfields. Particularly, the work of Babinsky et Al. highlights similar flow structures in case of an SBLI interaction generated by a full span wedge.(Babinsky et al., 2013) In that case the primary separated region exhibits much stronger recirculation. Similar oil flow results are shown in the work Xiang and Babinsky. (Xiang & Babinsky, 2019) Based on these results it is also expected that the corner flow interaction will propagate downstream of the primary shock impingement, although the extent and strength of this shock at that point in the flow is unknown.

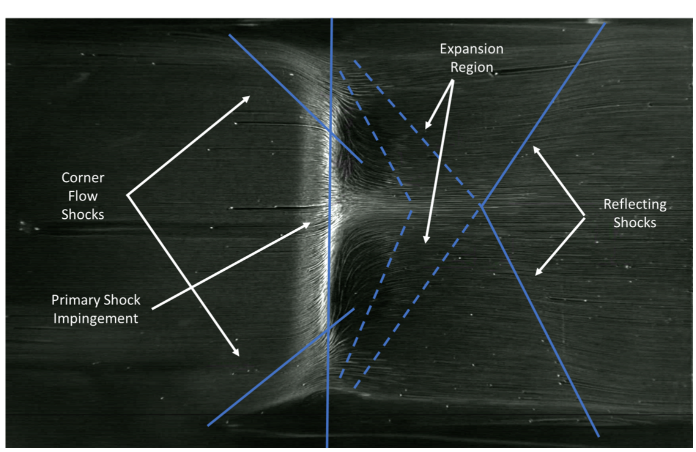

Figure 10. Oil flow visualization with shock interaction overlaid

3.2. PSP

Pressure sensitive paint results for the same oblique shock interaction are show in Figure 11.

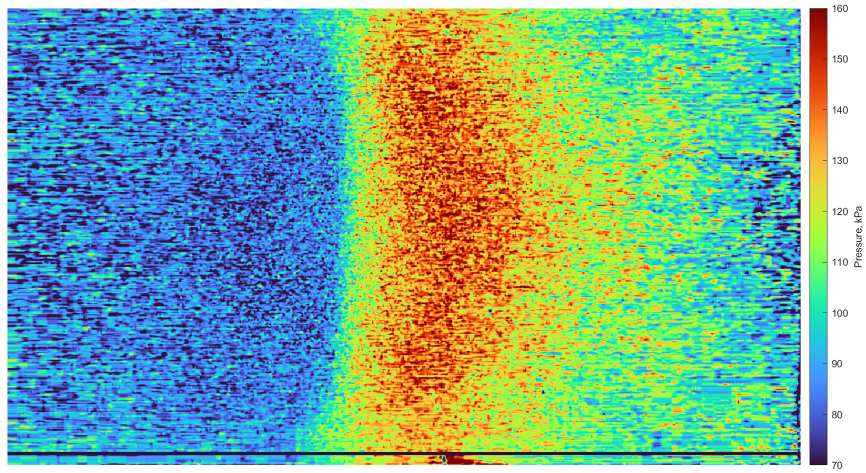

Figure 11. Calibrated pressure field of an oblique shock impingement at Mach 2.0

Here, the upstream pressure appears uniform suggesting a satisfactory image flattening. The initial shock impingement pressure rise exhibits good two-dimensionality across the center half of the test section. There is a slight asymmetry to the resulting OFV and PSP patterns likely due to misalignment of the test article. The corner flow separation apparent in the OFV results is also readily apparent in the PSP results. It is clear however based on both the OFV and PSP that the streamwise extent of this quasi-separated flow region appears to vary greatly in the span-wise direction, appearing as a crescent shaped region of peak pressure in the previously shown results. The work of Xiang and Babinsky indicates a similar form of the separated region pressure field. The pressure rise generated by the semi-span oblique shock in this work is less than that for the full span wedge used in that work. The shock pressure rise appears weaker in the corners than at the centerline. Further downstream, static pressure appears near the original static pressure upstream, perhaps owing to the narrow span-wise width of the detached shock region upstream. Two residual bands of high pressure can be seen extending diagonally away from the centerline towards each wall downstream of the main shock interaction region. These bands coincide with the shocks indicated by the OFV results. The same shock interaction presented previously is overlaid on the PSP data to correlate the shock structure and pressure rise. This is shown below in Figure 12.

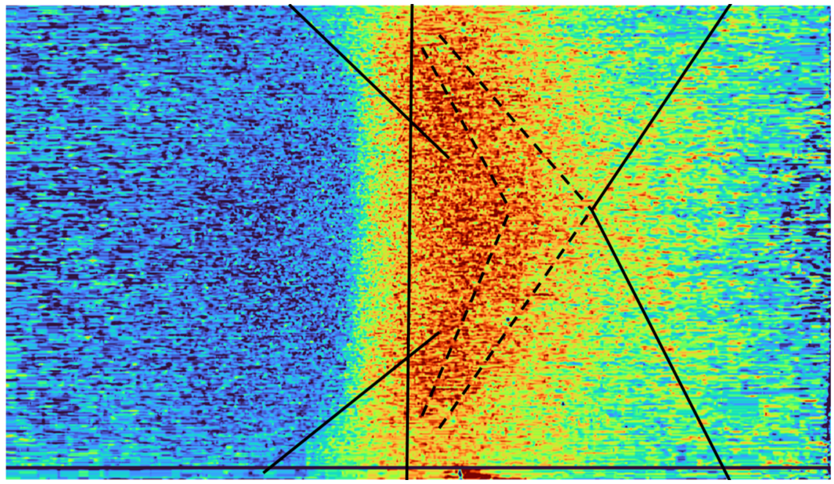

Figure 12. PSP image with shock interaction overlaid

4. Conclusions

With this work, the foundation has been laid for performing optically based, minimally invasive flow measurements in realistic internal flows. The challenges of maintaining a compact package, ensuring simple integration, and maintaining low cost were adressed via the camera housing and supporting hardware system described previously. An overview of the developed system has been presented detailing all necessary components and a viable method for camera integration. The system was applied to a practical flowfield, that of an oblique shock SBLI at Mach 2.0. The primary flow features were identified and discussed in light of recent research in this field.

While this system was successful, there is still much to be desired. Developing a system based around a higher frame rate and higher resolution image sensor than the one used in this work would offer the ability to capture finer flow details and approach quasi-time resolved measurements.

5. Future Work

To expand on the ground work laid here, a camera system with higher frame rate and resolution will be integrated into a Busemann inlet test article for testing in the University of Tennessee Space Institute (UTSI) Tennessee Aerothermodynamics Laboratory (TALon) Mach 4.0 Ludwieg tube facility. This system will be used to visualize the shock train impingement generated within the inlet-isolator system at various angles of attack and backpressure conditions via PSP and UV-OFV.

Acknowledgements

This work was funded under AFRL Enhanced Technology for Hypersonic Operable Systems (ETHOS) Contract No. FA8650-20-C-2406.

The authors would also like to thank Tom McManus of AFRL RQHX and Daniel Stubbs of the Auburn University Combustion Physics Laboratory (AUCPL) for their help in producing figures for this work.

Nomenclature

I	Image sensor intensity
m, n	Image sensor coordinates
P	Static pressure [kPa]
Re_L	Reynolds number per unit length [1/m]
δ	Flow turning angle, [Deg.]
β	Shock wave angle, [Deg.]
AR	Tunnel aspect ratio, W/H
P_0	Stagnation pressure, [kPa]
P_2/P_1	Inviscid shock pressure rise
M	Mach number

References

Arducam. (2020). *Arducam ov9281 1mp monochrome global shutter camera module with m12 mount lens for raspberry pi 4/3b+/3.* https://www.arducam.com/product/ov9281-mipi-1mp-monochrome-global-shutter-camera-module-m12-mount-lens-raspberry-pi/.

Babinsky, H., Oorebeek, J., & Cottingham, T. G. (2013). Corner effects in reflecting oblique shock-wave/boundary layer interactions. *51st AIAA Aerospace Sciences Meeting including the New Horizons Forum and Aerospace Exposition 2013*(January), 1–10. doi:

Davis, B. P. (2013). *Design and construction of a mach 2.0 wind tunnel for cavity acoustics research .*

Emami, S., Trexler, C., Auslender, A., & Weidner, J. (1995). *Experimental investigation of inlet-combustor isolators for a dual-mode scramjet at a mach number of 4* (Tech. Rep.).

Innovative Scientific Solutions, I. (2020). (Tech. Rep.). 7610 McEwen Road, Dayton, OH 45459. Retrieved from https://innssi.com/single-component-pressure-sensitive-paints/

Jahanmiri, M. (2011). *Pressure Sensitive Paints: The Basics & Applications* (Tech. Rep.). Goteborg, Sweden: Chalmers University of Technology.

Omnivision. (2020). Retrieved from https://www.ovt.com/products/#image-sensor

Sony. (2020). *Image sensor : products || sony semiconductor solutions group.* Retrieved from https:// www.sony-semicon.co.jp/e/products/IS/

Tsukahira, T., Wong, W., & Franco, B. (1971). *Supersonic inlet investigation* (Tech. Rep. No. AD0891376).

Wagner, J. (2009). *Experimental studies of unstart dynamics in inlet/isolator configurations in a mach 5 flow .*

Xiang, X., & Babinsky, H. (2019). Corner effects for oblique shock wave/turbulent boundary layer interactions in rectangular channels. *Journal of Fluid Mechanics*, *862*, 1060–1083. doi: